nature communications

Article

https://doi.org/10.1038/s41467-026-70098-8

Stretch-induced reversible self-growth of high aspect ratio microstructures scribed by femtosecond laser

Received: 19 July 2025

Accepted: 18 February 2026

Yachao Zhang[1,8], Nian Zhang[2,8], Dong Wu[3], Zehang Cui[4], Zhicheng Zhang[3], Tongzhang Wang[1], Rui Xu[1], Kejia Lu[1], Zhaoxin Lao[1], Sizhu Wu[1] ✉, Jiawen Li[3], Liu Wang[2], Ying Li[5], Li Zhang[6], Jiaru Chu[3] & Yanlei Hu[3,7] ✉

Inspired by the intricate surface patterns in nature, the concept of polymer self-growth has recently been applied to construct synthetic structures. However, existing techniques, whether driven by chemical reactions or physical mass transport, fail to offer rapid and reversible tuning, and typically can only produce structures with low aspect ratios. Here, we present a generalized stretch-induced polymer self-growth (SIPS) method for reversibly constructing structures on a wide range of pre-stretched elastic membranes, including silicone, PU, PDMS, dielectric elastomer (VHB), and hydrogel. High aspect ratio (~1.4, much larger than the previously reported value ~ 0.25) straight and bent micropillars with different cross-sections are facilely fabricated by femtosecond laser cutting. By releasing and subsequent re-stretching the membrane, tuning of the grown structures is readily achievable, enabling a rapid (~ 30 s) and reversible transition between structured and flat surface. Experimental and simulation results confirm that the micropillar height is governed by the stretch ratio and laser scribing depth. The high aspect ratio enhances tactile perception and allows directional bending for encoding information. These capabilities are demonstrated through proof-of-concept applications in Braille training and information encryption/decryption. The presented SIPS method that combines femtosecond laser cutting and the stretching of elastic membranes, offers an efficient approach for fabricating tunable functional microstructures with great potential in the fields of micro/nanofabrication and adaptive surface engineering.

Organisms in nature have evolved unique micro- and nanostructures that can reversibly change their shapes, enabling functions such as switchable friction[1–3], reversible adhesion[4–6], and adaptive camouflage[7–9]. Such intriguing microstructures are spontaneously formed through a growth mode, where living creatures absorb nutrients and integrate them into their bodies. Inspired by these natural patterns, artificial structures are typically fabricated using subtractive or additive methods, including cutting[10], molding[11,12], and printing[13]. While these patterning technologies offer high-fidelity processing capabilities, challenges such as tool wear, damage to the mold, and the necessity for harmful substances limit their sustainability. Moreover, the fabricated structures usually have fixed morphologies, making it difficult to meet the requirements of tunable function.

Inspired by dynamic and nonequilibrium systems in nature[14,15], researchers have recently developed chemically driven polymer self-growth to construct synthetic microstructures[16–26]. For instance, Cui et

A full list of affiliations appears at the end of the paper. ✉e-mail: sizhuwu@hfut.edu.cn; huyl@ustc.edu.cn

al. reported a UV light-regulated method that couples photolysis, photopolymerization, and transesterification to drive nutrient solutions into the irradiated region, where they polymerize and form microprotrusions[16]. Such chemically driven polymer self-growth strategies have greatly advanced micropatterning technologies, with demonstrated applications in structural color[27], biomedical implant[28], and hydrogel sensors[29]. However, these methods share several intrinsic limitations: (1) They require complex chemical compounds, such as photoresponsive polymers, polymerizable substances, and harmful solvents or reactants, which lead to multi-step pre-treatment processes and strict reaction conditions. (2) The growth rates are extremely slow, constrained by both the kinetics of the chemical reactions and the diffusion rates of the involved compounds, with average speeds ranging from tens of nm/s to several μm/s[16–22]. In addition, although several studies[17,20] have reported reversible control over the grown structures, these approaches remain limited by slow tuning speeds, reliance on specific materials, and stringent conditions. (3) Structures are limited to straight microprotrusions with a low aspect ratio (<0.3) due to the constraint imposed by the substrate, making it even more challenging to achieve the bending of microstructures. A detailed comparison is provided in Table S1.

As an alternative to chemical approaches, our group developed a physical mass transport-based method termed laser-induced polymer self-growth (LIPS)[30,31]. Utilizing this approach, micropillars and mushroom-like reentrant microstructures can spontaneously grow from a heat shrinkable shape memory polystyrene membrane. However, LIPS is only applicable to shape memory polymers, and the resulting structures cannot be reversibly tuned, which limits its applications. Therefore, developing a simple and general method to achieve fast and reversible tuning of self-grown structures with high aspect ratio remains a significant challenge.

Here, we report a strategy termed stretch-induced polymer self-growth (SIPS), which enables rapid and reversible fabrication of high aspect ratio structures on various elastic membranes. By precisely controlling femtosecond laser scribing to locally release stress, both symmetrical and asymmetrical polymer growth can be initiated, enabling the fabrication of straight and bent micropillars. The resulting structures achieve aspect ratios up to 1.4. The micropillar height is governed by the stretching ratio and laser scribing depth, and the growth speed reaches 130 μm/s, which is two orders of magnitude faster than that of chemically driven self-growth methods[16–22]. Upon releasing and re-stretching the membrane, the height, spacing, and bending angle of the grown micropillars can be facilely tuned, allowing for the rapid and reversible tuning between structured and flat surfaces. Micropillar growth, bending, and morphological evolution under cyclic releasing and stretching are systematically studied, and the simulation results exhibit excellent agreement with experimental observations. As a proof-of-concept, the tunable high-aspect-ratio structures are applied to Braille training and information encryption/decryption. The proposed method is general and compatible with various elastic membranes, including silicone, PU, and PDMS, and offers a versatile platform for constructing tunable surfaces in micro/nanofabrication technologies.

Results

Mechanism of stretch-induced polymer self-growth (SIPS)

As shown in Fig. 1a, a commercially available silicone membrane is first cut into a symmetrical cruciform shape and biaxially stretched by 30 mm in both directions to introduce a stretching ratio of $\lambda = 1.67$ (Video S1 and Fig. S2). A femtosecond laser is then used to ablate the membrane along the 2D circular paths. During laser scribing, a 3D micropillar grows out of the flat surface at a speed of ~130 μm/s (Video S2). Notably, the SIPS-fabricated micropillars exhibit a maximum aspect ratio of 1.4, which is higher than those produced by chemically driven self-growth techniques[16–22]. When the applied stress is released, the micropillars gradually disappear into the membrane. The detailed reversible self-growth process is demonstrated with schematics, simulations, and experiments in Fig. 1b and Video S3. The simulation confirms that the stress is uniformly distributed in the central region of the stretched membrane (Fig. S3). Laser ablation causes localized separation of material from the surrounding matrix in the *x-y* plane, which releases stress and induces centripetal shrinkage toward the center, leading to the formation of a micropillar (Fig. S4). The microscope images of a micropillar with increasing laser scribing depth (H_2) demonstrate the self-growth process, and the simulations align well with the experimental results (Fig. S5). Upon gradual relaxation to $\lambda = 1$, the matrix material surrounding the micropillar recovers to its original thickness, making the micropillar appear embedded within the substrate and restoring the surface to a flat state. Reapplying the stress allows the micropillar to be reversibly formed again (Video S4). Analyses of the radial stress distribution (Fig. 1c and Fig. S6) and cross-sectional profile (Fig. 1d and Fig. S6) from the simulation results show that as H_2 increases from 0 to 166 μm, internal stress within the scribed region gradually decreases to zero, while its height (H_1) increases, resulting in well-defined micropillar.

Compared to our previously reported LIPS method, which is limited to heat shrinkable shape memory polymers[30,31] and irreversible structures, the SIPS method enables reversible structural tuning and is applicable to various elastic materials, including Polyurethane (PU), Polydimethylsiloxane (PDMS), Dragon Skin 10 silicone elastomer mixed with carbon nanotubes, dielectric elastomer (VHB) and hydrogel (Fig. S7–8). Moreover, owing to its athermal nature, SIPS achieves finer features with diameters down to 15 μm, significantly smaller than the 150 μm minimum feature size achievable with LIPS (Fig. S9). While one report has demonstrated a chemical self-growth feature size as small as 0.75 μm[17], the vast majority of chemical self-growth methods typically produce structures within the 100–500 μm range[16,18,20–22]. In contrast, SIPS enables rapid, reversible fabrication of high-aspect-ratio structures with fine feature sizes (~15 μm) using standard elastomers without chemical pretreatment, expanding its potential for precise and scalable microfabrication.

Stretch-induced self-growth of straight micropillars

The formation process of the micropillar is investigated by using femtosecond laser to continuously scribe along a circular path with a diameter of 360 μm (Fig. 2a). The number of laser scanning cycles is varied from 0 to 80, increasing the scribing depth (H_2) from 0 to 166 μm. SEM images show the evolution of the micropillars and the large-scale micropillar arrays (Fig. S10). Corresponding cross-sectional profiles of the structures (Fig. 2b) show that the micropillars have sharp sidewalls, with a taper ratio as low as 0.098. Based on morphological changes, the evolution process of the micropillar is divided into four stages. In the first stage ($H_2 < 18$ μm), the interior of the circular region remains flat. In the second stage (H_2 ranging from 18 to 38 μm), the material near the scribing path contracts inward, while the central region remains flat, forming an inversed-bowl-shaped structure. In this stage, the structure is still within the matrix. In the third stage (H_2 ranging from 38 to 54 μm), the structure begins to protrude from the flat surface, with the material in the central region being lower than the periphery, forming a crater-like shape. In the fourth stage ($H_2 > 54$ μm), the top central part of the structure reaches the same height as the periphery, forming a micropillar. As the laser ablation continues, more material contracts toward the center, and the micropillar grows higher. Quantitative analysis from the confocal cross-sectional profiles and simulation results reveals that as H_2 increases, the diameter of the microstructure (D) decreases from 300 to 220 μm and then stabilizes, while the height (H_1) increases up to 232 μm (Fig. 2c). After complete release of the membrane stress (Fig. 2d), only small bumps remain on the surface, corresponding height profile and sizes are shown Fig. 2e, f, respectively. The maximum height of the bump is ~7.7 μm at 80 cycles,

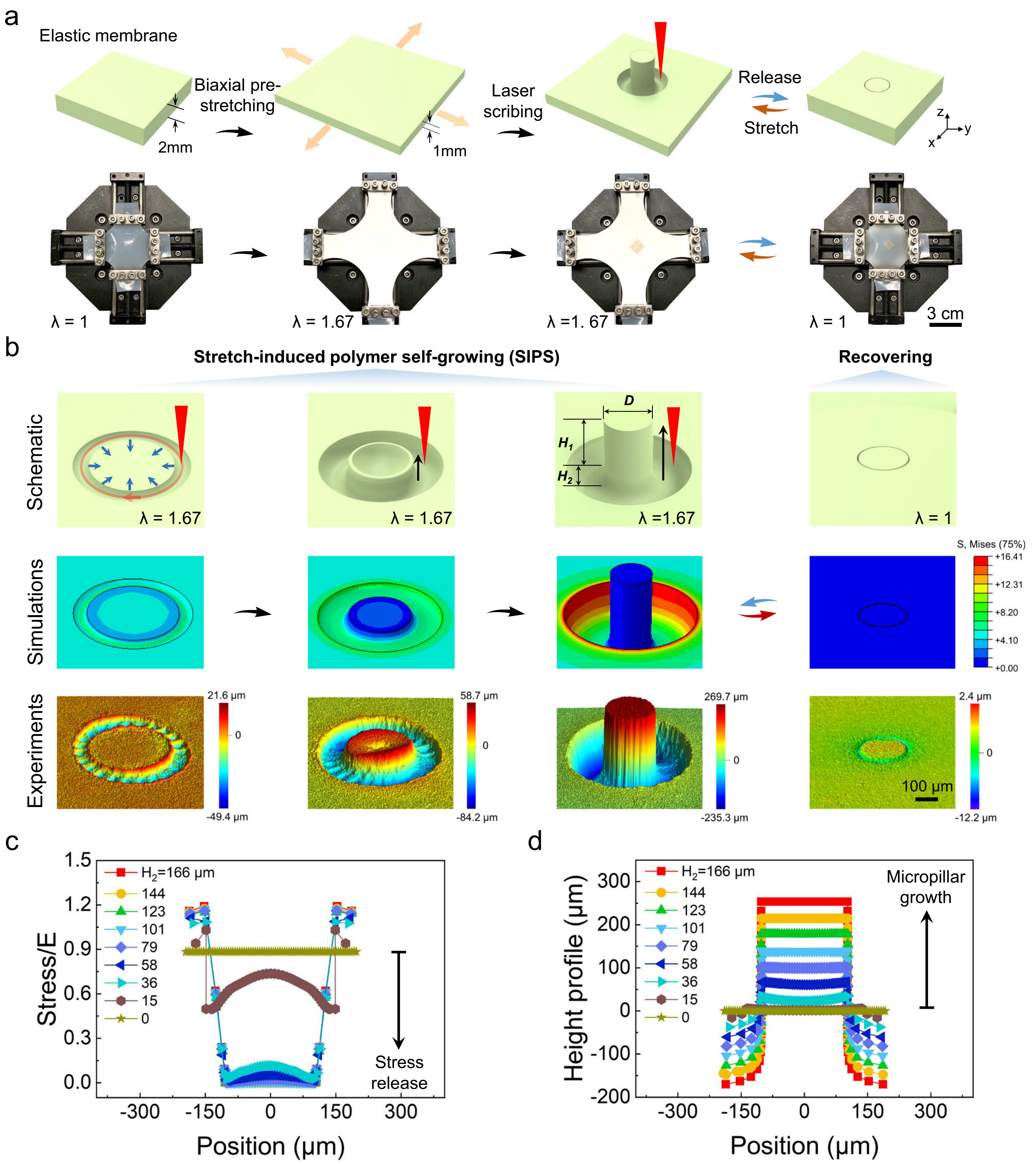

Fig. 1 | Mechanism of stretch-induced polymer self-growth and reversible tuning of microstructures. a Schematic and experimental demonstration of stretch-induced polymer self-growth (SIPS) of microstructures on a biaxially stretched silicone membrane. **b** Schematic, simulation, and experimental validation of the SIPS process and its subsequent reversible tuning. The parameters λ, H_1, H_2, and D represent the stretching ratio, micropillar height, laser scribing depth, and micropillar diameter, respectively. **c** Finite element simulation results of radial stress distributions in the grown microstructures as laser scribing depth increases from 0 to 166 μm. **d** Simulated cross-sectional profiles of grown microstructures corresponding to varying laser scribing depth.

and the diameters are nearly unchanged. Benefiting from the flexibility of femtosecond laser processing, various 2D geometries, such as square and heart shapes, are utilized to fabricate micropillars with diverse shapes (Fig. S11).

To quantitatively investigate how the stretching ratio (λ) and laser scribing depth (H_2) influence micropillar morphology, the self-growth process is simulated under various combinations of λ and H_2. Contour maps of the H_1 and D are obtained by measuring the sizes of the simulated self-grown micropillars (Fig. 2g, h). Experimental results under five representative conditions ($H_2 = 60$ μm, $\lambda = 1.18$; $H_2 = 80$ μm, $\lambda = 1.27$; $H_2 = 100$ μm, $\lambda = 1.34$; $H_2 = 120$ μm, $\lambda = 1.54$; $H_2 = 140$ μm, $\lambda = 1.67$) show excellent agreement with the simulations (Fig. 2i, j). This consistency confirms the predictive capability of the simulation framework and highlights its utility in guiding structural

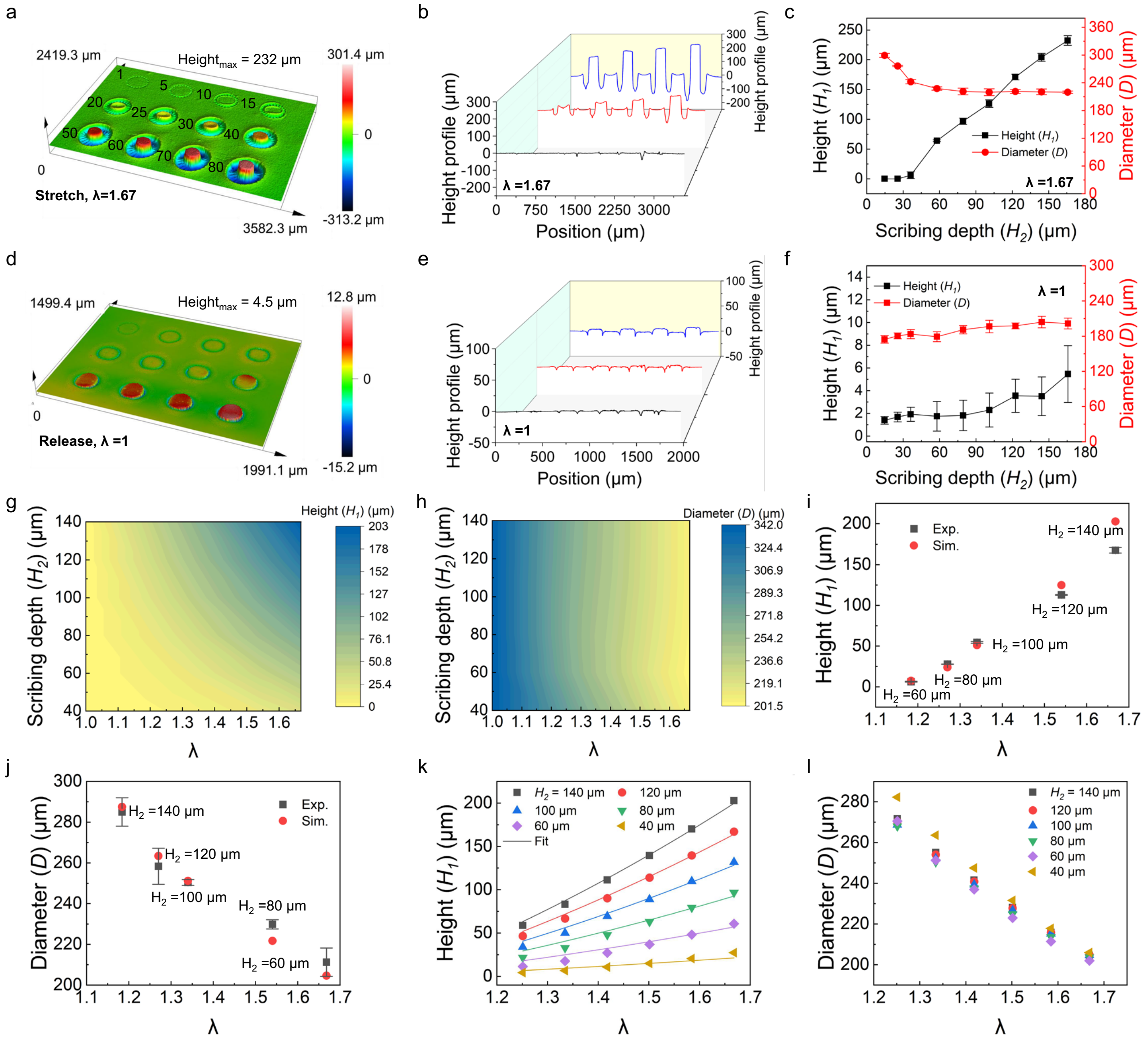

Fig. 2 | Stretch-induced self-growth of straight micropillars. **a** Laser confocal image of straight micropillars fabricated with increasing scanning circles from 1 to 80 on the biaxially stretched membrane (stretching ratio λ = 1.67). **b** Corresponding cross-sectional profiles of straight micropillars shown in (**a**). **c** Experimental results of micropillar height and diameter as a function of laser scribing depth. **d** Laser confocal image of microstructures in (**a**) after completely releasing the membrane. **e** Corresponding cross-sectional profiles of microstructures shown in (**d**). **f** After releasing the membrane, the experimental results of micropillar height and diameter as a function of laser scribing depth. Contour maps of micropillar height (**g**) and diameter (**h**) as functions of both laser scribing depth and stretching ratio. Comparison between experimental and simulated results of micropillar height (**i**) and diameter (**j**) under five experimental conditions: H_2 = 60 μm, λ = 1.18; H_2 = 80 μm, λ = 1.27; H_2 = 100 μm, λ = 1.34; H_2 = 120 μm, λ = 1.54; H_2 = 140 μm, λ = 1.67. Quantitative relationships between micropillar height (**k**) and diameter (**l**) with the stretching ratio at different laser scribing depths according to the simulation results. Error bars represent the standard deviation of three independent measurements.

design, thereby reducing the need for laborious experiments and characterizations.

Given the near-zero taper ratio (0.098), the micropillars are approximated as cylinders. Considering the volume of the material is conserved during self-growth, the height of the micropillars H_1 is found to be proportional to λ^2–1 and H_2 (Fig. S12). By extracting data from the contour maps, the quantitative relationship between H_1 and λ at different H_2 (Fig. 2k), as well as the quantitative relationship between H_1 and H_2 at different λ are obtained (Fig. S13). We find that the relationship can be fitted by the equation $H_1 = (\lambda^2–1)\ (H_2\text{-}28)$. This indicates that structure protrusion occurs only when $\lambda > 1$ and H_2 exceeds 28 μm (for a scribing diameter of 360 μm), and the H_1 is proportional to both the λ^2–1 and H_2, which is consistent with the theoretical prediction (Fig. S12).

Additionally, by extracting data from the contour maps, the quantitative relationship between diameter of micropillar D and λ at different H_2 (Fig. 2l), as well as the quantitative relationship between D and H_2 at different λ are also obtained (Fig. S13). The results show that under the same scribing depth, increasing λ leads to a reduction in D. Similarly, as the H_2 increases, the D gradually decreases and eventually stabilizes. The final stabilized D value is inversely proportional to the λ. Moreover, FEA and experimental results show that varying the Young's modulus (E) across a wide range has no effect on the self-grown micropillar dimensions (Fig. S14-15). This observation confirms that the micropillar morphology is governed by the pre-stretch ratio and laser scribing depth, and is irrelevant with the material stiffness.

The accessible stretching ratio λ in SIPS is constrained by the mechanical properties of the elastomeric substrate. First, the fracture

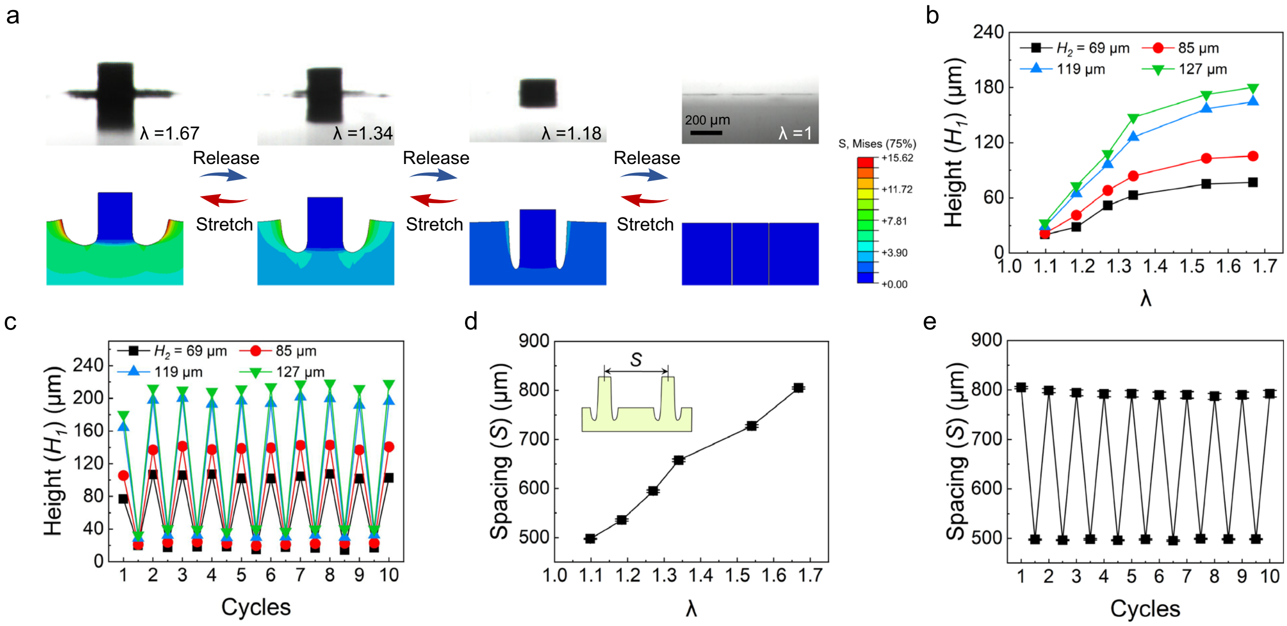

Fig. 3 | Reversible tuning of stretch-induced self-grown straight micropillars. **a** Side view optical images and corresponding simulations of a micropillar varying stretching ratio from 1.67 to 1. **b** Heights of micropillars fabricated at laser scribing depths of 69, 85, 119, and 127 µm varies as a function of stretching ratio. **c** Cyclic variation in micropillar height during ten successive cycles of release and re-stretching, corresponding to the four structures shown in (**b**). **d** Spacing of the micropillars in (**b**) as a function of stretching ratio. **e** Spacing variation of micropillars in (**b**) during ten cycles of release and re-stretching. Error bars represent the standard deviation of three independent measurements.

elongation (F) defines an upper limit, since λ must remain below the fracture strain to avoid macroscopic failure (Fig. S16). The measured elongations at break are approximately 275% for silicone, 500% for PU, and 125% for PDMS, corresponding to maximum stretch ratios of $\lambda \approx 3.75$, 6.0, and 2.25, respectively. Second, the effective stretching ratio accessible for SIPS is governed by the deformation regime of the material. Unlike metals, elastomers do not exhibit a distinct yield point and instead undergo a continuous transition from elastic-dominated deformation to viscoelastic dissipation at large strains[32], which is reflected in the strain-dependent slope (tangent modulus) of the stress–strain curves[33].

Silicone exhibits a smooth stress–strain response with only modest variation in tangent modulus over a wide strain range, indicating predominantly elastic-dominated deformation (Fig. S16). In contrast, PU shows a reduction in tangent modulus at intermediate-to-large strains due to dissipation-dominated deformation, as reported for polyurethanes[34]. PDMS exhibits a pronounced increase in tangent modulus at large strains due to strain hardening associated with finite chain extensibility, consistent with established constitutive models of rubber elasticity[35]. When yield-like deformation in PU and PDMS becomes significant, part of the applied stretching may become irreversible, which can compromise the reversibility of the self-grown microstructures and hinder complete retraction of the micropillars into the substrate upon release. Owing to its predominantly elastic-dominated response, silicone is therefore a favorable substrate for SIPS-induced self-growth.

Reversible tuning of stretch-induced self-grown straight micropillars

To investigate the tuning behavior of micropillars during release and re-stretching, a row of micropillars fabricated at different laser scribing depths (H_2 = 69, 85, 119 and 127 µm) under a stretching ratio (λ) of 1.67 is subjected to cyclic deformation. Side-view images captured during gradual relaxation from $\lambda = 1.67$ to 1.0 reveal a progressive decrease in pillar height (Fig. 3a, Fig. S17), which is consistent with simulation results. As shown in Fig. 3b, for the micropillar fabricated at H_2 = 127 µm, the H_1 decreases from 180 to 32 µm as λ is reduced from 1.67 to 1.098. The other three micropillars fabricated at H_2 of 69, 85 and 119 µm exhibit the same trend of H_1 reduction during release. Upon reapplying equibiaxial stretching to the membrane, the micropillars exhibit a noticeable increase in height compared to their post-release state (Fig. 3c). This increase occurs primarily during the first re-stretching cycle, which is attributed to localized geometric discontinuities introduced by prior laser scribing. The scribed grooves act as mechanically compliant regions that deform more readily than surrounding material (Fig. S6), leading to tearing and expansion of both groove depth and width (Fig. S18). In subsequent stretching–release cycles, the micropillar height remains unchanged, indicating that the structure reaches a mechanically stable configuration, as further confirmed by the additional cyclic durability results shown in Fig. S19.

As the pre-stretch ratio decreases from 1.67 to 1.098, the spacing between adjacent micropillars reduces from 805 to 497 µm (Fig. 3d). Notably, the micropillar spacing remains constant throughout all stretching–release cycles (Fig. 3e), confirming the geometric reversibility and mechanical stability of the self-grown micropillars.

Stretch-induced self-growth and reversible tuning of bent micropillars

In addition to the straight micropillars, bent micropillars can be fabricated using an asymmetric laser scribing strategy (Video S5). As shown in the schematic and simulation results (Fig. 4a and Video S6), a straight micropillar is first prepared with H_2 of 105 µm, and then a semicircular path is scribed repeatedly on one side of the micropillar with an additional laser scribing depth of H_3, introducing asymmetric stress release. This localized imbalance causes the asymmetric growth, with the micropillar bending towards the other side that is not scanned. A variety of ordered patterns composed of bent micropillars with controlled pillar numbers, spatial arrangements, and bending directions are successfully fabricated (Fig. S20). By releasing the silicone membrane, the bent micropillars retract into the matrix. When re-stretched, the bent micropillars reappear on the surface,

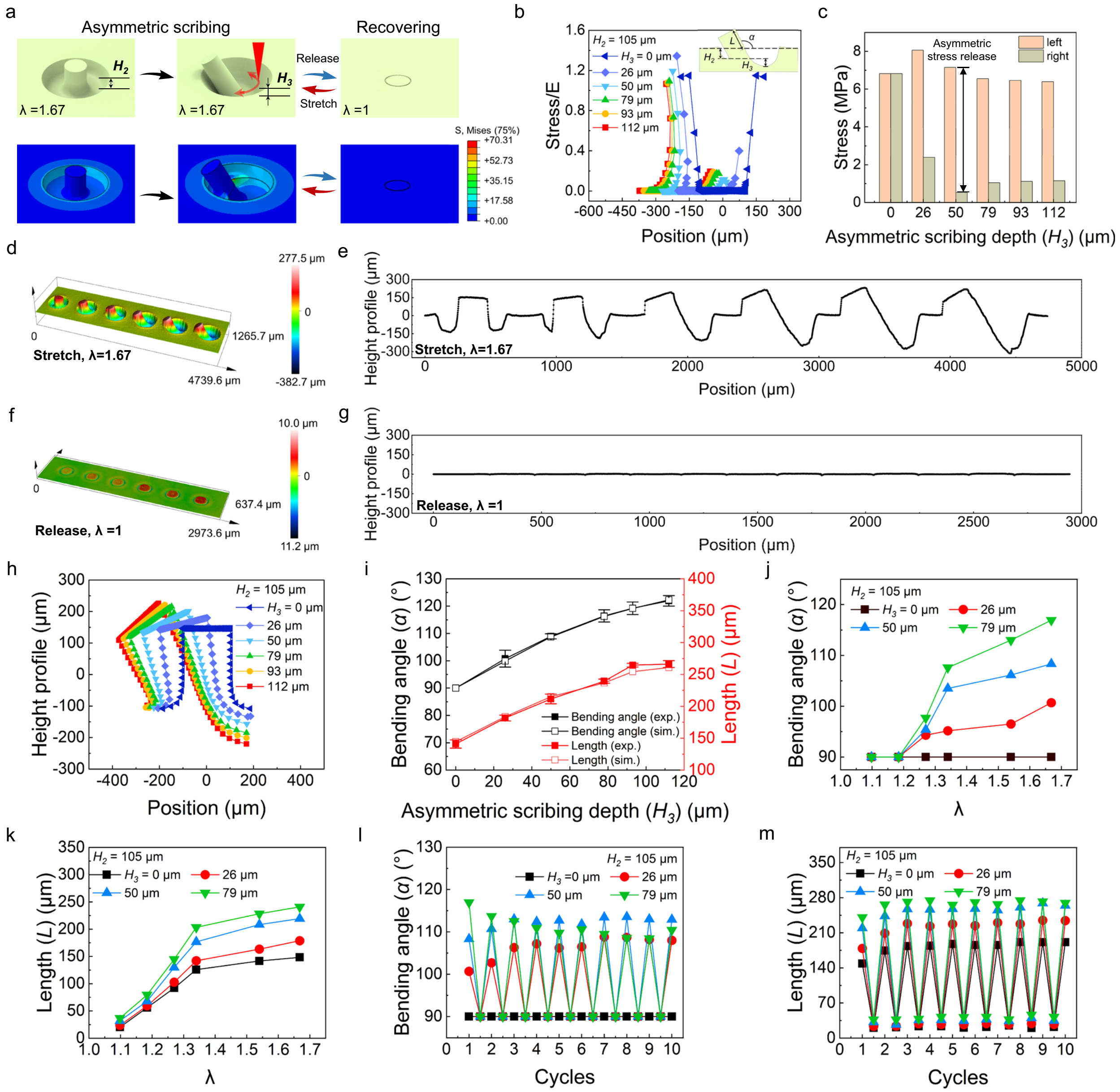

Fig. 4 | Stretch-induced self-growth and reversible tuning of bent micropillars. **a** Schematics and simulations illustrating the fabrication and reversible tuning of bent micropillars. H_2 and H_3 represent the laser scribing depths corresponding to circular and semicircular paths, respectively. **b** Simulated radial stress distributions of the bent micropillars fabricated with varying H_3. Bending angle (α) and micropillar length (L) are defined in the illustration. **c** Comparison of the stresses at the left and right roots of the bent micropillars shown in (**b**). **d** Laser confocal image of the bent micropillars fabricated with increasing H_3 at stretching ratio of 1.67. **e** Corresponding cross-sectional profiles of bent micropillars in (**d**). **f** Laser confocal image of microstructures in (**d**) after full release of the membrane. **g** Cross-sectional profiles of microstructures in (**f**). **h** Simulated height profiles of bent micropillars with the increasing H_3. **i** Experimental and simulation results of bending angle (α) and length (L) of micropillars as a function of H_3. The variation in the bending angle (**j**) and length (**k**) of the micropillars fabricated with increasing H_3 during release. The variation in the bending angle (**l**) and length (**m**) of the micropillars fabricated with increasing H_3 during ten cycles of release and re-stretching. Error bars represent the standard deviation of three independent measurements.

demonstrating reversibility (Video S7). The radial stress distributions of the bent micropillars are obtained from simulation results (Fig. 4b and Fig. S21). A comparison of stresses at the left and right roots of the bent micropillar confirms that bending is driven by asymmetric stress release (Fig. 4c). A series of bent micropillars is fabricated with increasing H_3 (Fig. 4d), and cross-sectional profiles show that the bending angle (α) increases with the H_3 (Fig. 4e). After full stress release, only small bumps remain (Fig. 4f, g), with the height and diameter of ~4 μm and ~205 μm, respectively. Reapplying the same stretching ratio to the membrane, the micropillars reappear with the same bending trend as before (Fig. S22). The simulated profiles of bent micropillars with increasing H_3 show the same increasing bending angle as observed with experiments (Fig. 4h). The quantitative relationship between H_3 and both bending angle and length (L) of the micropillars are shown in Fig. 4i. As H_3 increases, the bending angle rises from 90° to 122°, while the length extends from 141 μm to 266 μm. These trends confirm excellent agreement between simulations and experiments.

The tuning behavior of bent micropillars during release and re-stretching is further investigated. A row of bent micropillars, initially fabricated with a H_2 of 105 μm to prepare straight micropillars, is further processed with H_3 of 0, 26, 50 and 79 μm. These are designated as B-0, B-26, B-50 and B-79, respectively. After being subjected to release and re-stretching cycles, side-view images at different stretching ratios are shown in Fig. S23. As λ decreases from 1.67 to 1.098, all bent micropillars exhibit reduced bending angles and tend to become straight (Fig. 4j). Upon re-stretching to $\lambda = 1.67$, B-0 remains straight, while B-26 and B-50 exhibit increased bending angles (Fig. S23). This behavior is attributed to the aforementioned localized tearing at the laser-scribed microgrooves. In contrast, B-79 shows a slight decrease in bending angle from 116.9° to 113.7°, likely due to the large H_3 making it more sensitive to deformation disturbances. Correspondingly, for B-0, B-26, B-50 and B-79, their lengths decrease during relaxation (Fig. 4k). In subsequent nine releasing-stretching cycles, B-0 remains straight, while the bending angles of B-26 and B-50 increase during the first seven cycles before reaching a plateau (Fig. 4l). For B-79, the bending angle decreases over the initial five cycles and then stabilizes. Correspondingly, the lengths of all micropillars increase during the first three cycles and subsequently remain constant (Fig. 4m). These trends are further confirmed by extended cyclic stretching–release tests up to 1000 cycles, as shown in Fig. S24. These results demonstrate that the morphology of the bent pillars can be reversibly tuned by controlling the stretching ratio. Additionally, smaller H_3 values are associated with improved recovery and mechanical reversibility.

In-situ micro-object capturing and releasing

The potential application of the SIPS method in in situ micro-object capture and release is demonstrated. As shown in Fig. S25 and Video S8, a claw-like structure composed of four inward-bending micropillars is fabricated around a SiO_2 microsphere, and the claw grasps the microsphere tightly. When air is blown using a rubber suction bulb, the microsphere captured by the claw-like structure remains immobile, whereas nearby unconstrained microspheres are easily removed. This indicates that the claw-like structure provides effective mechanical confinement and can resist external disturbance. By releasing the stress, the micro-claw gradually open and finally hides in the matrix, thereby releasing the microsphere. Furthermore, an array of such micro-claws is fabricated to simultaneously capture and release four microspheres (Fig. S26), demonstrating the scalability and programmability of this approach for micro-object manipulation.

Tunable Braille for beginning learners

Another potential application of the SIPS method is to assist beginners in learning and practicing Braille, a challenging and time-consuming process where any support should be seized upon. Braille is a widely used tactile writing system for people who are blind or visually impaired. Each Braille character is based on a 3 × 2 matrix, known as a Braille cell, composed of six dots that may either protrude or remain flat, resulting in 64 possible combinations. Previous studies suggest that enlarged Braille characters can help blind children transition into standard Braille more effectively[36,37]. However, the fixed dot size and spacing in current enlarged Braille may hinder a smooth transition, especially for beginners. This issue is particularly pronounced for individuals who acquire visual impairments later in life due to injury, illness, or aging. Their reduced fingertip sensitivity, compared to those born blind, makes Braille learning more difficult and discouraging, potentially undermining their learning motivation and confidence. To address these challenges, previous efforts have explored enlarged or tunable Braille devices, but these approaches still have significant limitations. For example, mechanically adjustable Braille displays can modify dot spacing by manually sliding a cover with preset hole arrays of different pitches, and adjust dot diameter by replacing point caps of varying sizes. However, these devices cannot adjust dot height, require manual intervention to change sizes, and typically display only a single character, greatly limiting training efficiency and user convenience[37]. Dynamic tactile displays with piezoelectric arrays support mode switching but offer only discrete, preset size options without continuous tuning, have fixed dot heights, and involve bulky and expensive setups unsuitable for everyday learning environments[38]. To date, no system enables simultaneous, continuous, and reversible adjustment of both dot height and spacing within a portable platform.

To overcome this limitation, we have developed a tunable Braille learning platform based on the SIPS method, which allows simultaneous and continuous adjustment of both dot pitch and dot height simply by stretching or releasing a silicone membrane. As illustrated in Fig. 5a, four Braille cells composed of micropillars are fabricated by SIPS method under a stretching ratio of 1.67. The Braille pattern represents the Chinese character "Ke Xue", meaning "Science". The design diameter of the circle is 1 mm, and the spacing is 2 mm. The resulting micropillars have a diameter of 510 μm and a height of 716 μm (aspect ratio ~1.4; Fig. S27). The high aspect ratio enhances tactile perception and improves Braille recognition accuracy, especially for beginners or individuals with reduced sensitivity. The micropillars remain intact after repeated finger contact under a normal force of 0.6 N (Video S9). A tactile recognition test is conducted with four first-grade and seven second-grade students from a special education school (Fig. 5b, c). Each student begins by touching the Braille at a low stretching ratio of 1.098. If they are unable to recognize the Braille, the stretching ratio is gradually increased until correct recognition is achieved, which is recorded as the critical recognition stretching ratio. Owing to individual differences in Braille learning duration and tactile sensitivity, the critical recognition stretching ratio varies among students (Fig. 5c). Notably, two first-grade students fail to recognize the Braille even at the maximum stretching ratio of 1.67, while one second-grade student successfully identified it at 1.098, indicating superior tactile perception. The experimental results suggest that the tunable Braille platform can be used to assess the proficiency of learners in Braille. In the future, this platform may assist Braille beginners by starting with an "easy mode" at higher stretching ratio, where enlarged dot spacing and height enhance tactile perception and build confidence. The stretching ratio can then be gradually reduced to help learners adapt to standard Braille, potentially accelerating the learning process (Fig. 5d). In addition, once the stress is completely released, the micropillars retract into the matrix, facilitating damage-free long-term storage and transportation.

To evaluate durability under practical operating conditions, we investigated the fatigue behavior of the Braille micropillar structures under two representative loading modes: repeated stretching–release cycles and repeated tactile contact (touching/friction) cycles. In stretching–release tests, the Braille-patterned membrane was subjected to 0–1000 cycles, and the scribing depth, micropillar height, diameter, and interpillar spacing were quantified (Fig. S28). During the first 200 cycles, minor material tearing at the laser-scribed grooves led to an increase in groove depth, accompanied by a corresponding increase in micropillar height, while the diameter and interpillar spacing remained essentially unchanged. Beyond 200 cycles, all geometric parameters reached a stable plateau and remained unchanged up to 1000 cycles.

To better emulate realistic Braille reading, cyclic tactile tests were performed using a custom-built friction platform (Fig. S29). A Dragon Skin 10 elastomer probe with a hemispherical radius of 8 mm was used to approximate fingertip geometry and compliance, and a normal load of 0.6 N was applied, consistent with reported Braille reading forces[39]. The sample was subjected to reciprocating friction along a fixed direction, with the sample rotated by 90° after each friction cycle. This procedure was repeated for up to 2000 cycles. During tactile cycling, the scribing depth gradually decreased as a result of substrate thinning induced by friction, while the micropillar height continuously increased from approximately 500 to 800 μm due to repeated compression and stretching imposed by the abrasion head. The micropillar diameter and the interpillar spacing remained unchanged throughout the entire process.

Overall, the Braille microstructures maintain a stable spatial arrangement and structural integrity under both cyclic stretching and

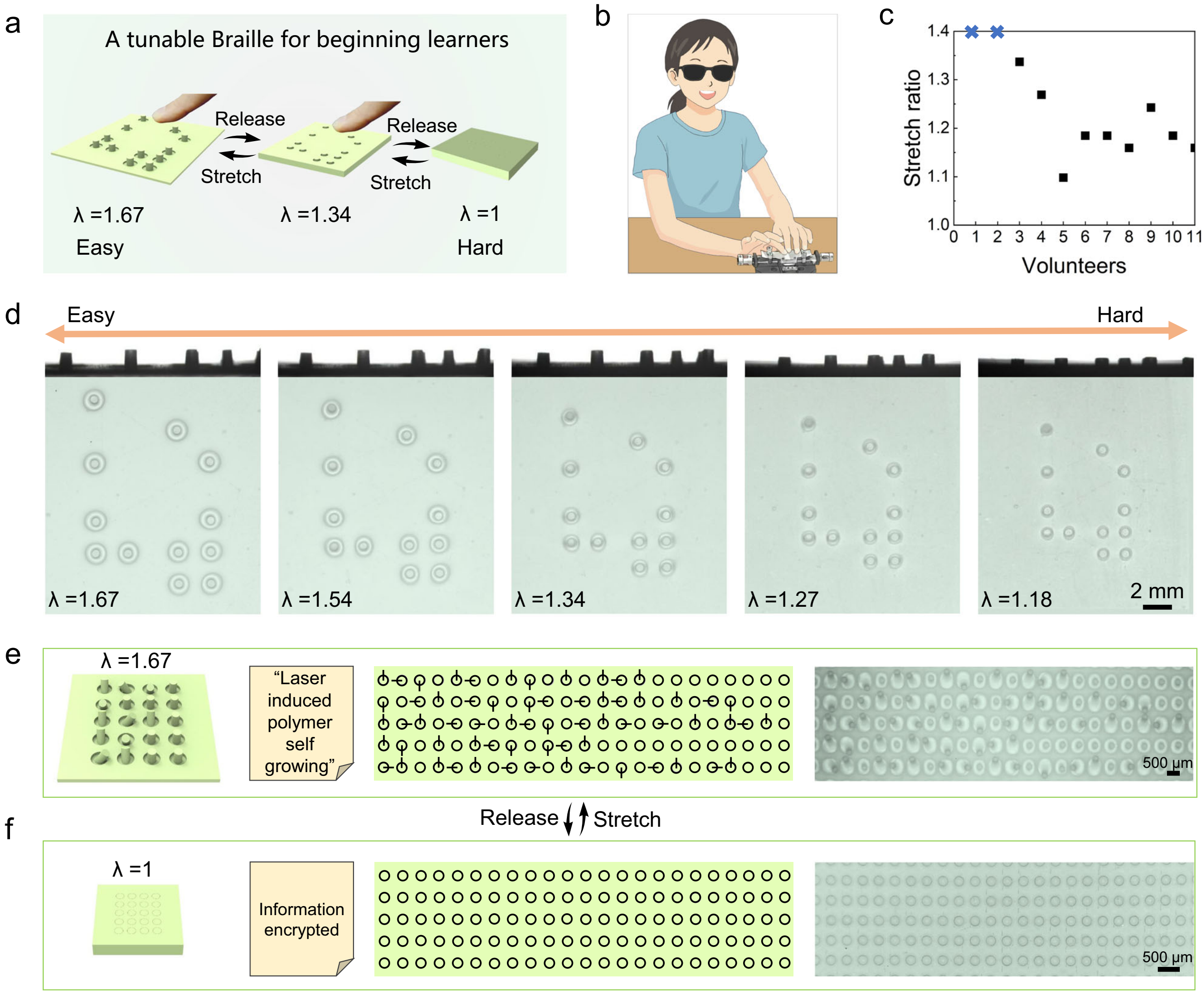

Fig. 5 | Applications of tunable Braille and information encryption/decryption. **a** Schematic illustration of Braille tuning by stretching or releasing the elastic membrane. **b** Schematic of primary school children testing Braille patterns with adjustable micropillar height and spacing. **c** Critical recognition stretching ratios vary among students, reflecting differences in tactile sensitivity and Braille proficiency. **d** Braille recognition difficulty can be modulated by adjusting the stretching ratio. Corresponding micropillar spacing and height are shown in side-view optical images. **e** At a stretching ratio of 1.67, the phrase "laser-induced polymer self-growing" is encoded into five rows of micropillars using four distinct bending directions. Straight micropillars are used to delimit characters. **f** Upon full release of the membrane, only laser ablation traces remain visible, rendering the encoded message temporarily invisible. Repeated release and re-stretching enable reversible information encryption and decryption.

repeated tactile loading, with no evidence of catastrophic fatigue failure within the tested ranges. Notably, repeated stretching–release cycles result in a modest increase in micropillar aspect ratio, while tactile loading induces a more pronounced increase, with the aspect ratio rising from ~0.94 to ~1.43. This behavior is enabled by the compliant deformation of the elastomeric micropillars, which accommodate repeated mechanical interactions through reversible bending and compression rather than material damage. As a result, the evolution toward higher-aspect-ratio Braille features is favorable for tactile perception, indicating that repeated use within the tested cycle range does not lead to functional degradation of the Braille training platform. It should be noted, however, that under much longer-term use involving tens or hundreds of thousands of tactile cycles, wear and material degradation of elastomeric substrates are expected to become unavoidable.

Information encryption and decryption

Beyond tactile applications, high-aspect-ratio micropillars allow information to be encoded through their bending orientations, as demonstrated by a modified Morse code scheme. The phrase "laser-induced polymer self-growing" is encoded using four distinct bending directions—upward, leftward, downward, and rightward—corresponding to dot, dash, double-dot, and double-dash, respectively (Table S30). Straight micropillars serve as delimiters between characters. At a stretching ratio of 1.67, the encoded message is clearly readable (Fig. 5e); when released to λ = 1, the micropillars retract and only laser ablation traces remain visible, effectively encrypting the information (Fig. 5f). This encryption–decryption process is shown to be reversible and repeatable over ten full stretching–release cycles (Video S10), confirming the robustness and reusability of the reconfigurable encoding platform.

Discussion

In summary, we propose a generalized and efficient stretch-induced polymer self-growth (SIPS) method for fabricating reversible microstructures on various elastic membranes. The approach demonstrates excellent material adaptability, allowing its application to diverse substrates including silicone, polyurethane (PU), polydimethylsiloxane (PDMS), dielectric elastomer (VHB), and hydrogel. High aspect ratio (~1.4) and well-defined (taper ratio <0.1) straight micropillars with different cross-sections, as well as complex surface patterns assembled by bent micropillars, can be rapidly prepared via femtosecond laser scribing at a growth speed up to 130 µm/s. Benefiting from the athermal nature of the process, the minimum feature size reaches 15 µm and may be further reduced by employing more precise techniques such as focused ion beam (FIB) etching. Such improvements in patterning resolution would enable finer control over local stress release and potentially allow submicron-resolution stress gradient modulation, thereby opening opportunities for the fabrication of more complex microstructures. The structural tunability is achieved by simply releasing and re-stretching the membrane, allowing surface morphologies to reversibly switch between flat and structured states within 30 seconds. This reconfigurability is experimentally validated and well-supported by simulations. The high aspect ratio is essential for functional applications, as it enhances tactile perception and enables programmable bending for multidirectional information encoding. These characteristics underpin practical demonstrations in Braille training and reversible information encryption/decryption. Compared to our previously reported laser-induced polymer self-growth (LIPS) method, which is limited to heat-shrinkable shape memory polymers and generates irreversible structures, the SIPS method significantly broadens the range of usable materials and enables reversible structural tuning.

Although the present work focuses on pristine elastomeric membranes, prior studies suggest that the incorporation of well-dispersed nanofillers could further enhance fatigue resistance and long-term durability[40,41]. Beyond mechanical reinforcement, multifunctional nanofillers—such as magnetic or photothermal nanoparticles—may impart additional stimulus-responsive or actuation functionalities to SIPS-generated microstructures. Such material-level functionalization, combined with the programmable self-growth enabled by SIPS, offers a promising route toward multifunctional soft microdevices and application-oriented extensions in future work.

Overall, our presented method combining femtosecond laser cutting and stretching of elastic membranes provides a robust and flexible platform for the rapid fabrication of reconfigurable microstructures, offering new opportunities in the fields of micro/nanofabrication, adaptive surfaces, and tactile interfaces.

Methods

Preparation of materials

Silicone membranes (thickness: 2 mm) were purchased from Pureshi in Taobao and cut into symmetrical cruciform shapes. Each silicone membrane was mounted on a custom-built biaxial stretching stage and stretched 30 mm in both directions using either manual or motorized rotating shafts. Silicon microspheres (diameter: 150–200µm) were purchased from Knowledge & Benefit Sphere Tech. Co., Ltd. A commercial acrylic dielectric elastomer film (VHB™ 4910, 3 M Company, USA) was employed as the dielectric elastomer substrate. Photo-crosslinkable poly(vinyl alcohol) (PVA)–based hydrogels were prepared by first dissolving PVA (0.2 wt%, molecular weight 75,000–79,000 g·mol^{-1}) in deionized water under magnetic stirring until complete dissolution. Subsequently, acrylamide (40 wt%), poly(ethylene glycol) diacrylate (PEGDA, 2 wt%), and a photoinitiator (Irgacure 2959, 1 wt%) were added to the solution and thoroughly mixed. The resulting precursor solution was injected into a mold and cured under ultraviolet illumination (365 nm) for 5 min to obtain a hydrogel film. Carbon nanotube (CNT)–doped elastomer samples were prepared using Dragon Skin™ 10 Slow silicone (Smooth-On). Briefly, CNTs (360 mg) were first dispersed in cyclohexane (25 mL) by magnetic stirring followed by ultrasonication for ~30 min, with intermittent water replacement to maintain the temperature below 30 °C, until a homogeneous black dispersion was obtained. The CNT dispersion was then added to Part A of Dragon Skin 10 Slow (29.82 g) and mixed thoroughly in a fume hood, allowing cyclohexane to evaporate completely. After solvent removal, an equal mass of Part B (29.82 g) was added and mixed uniformly. The mixture was subsequently degassed under vacuum to remove trapped air bubbles, cast into molds, and cured at 65 °C for 20 min to obtain CNT-doped elastomer films.

Stretch-induced polymer self-growth

A femtosecond laser system (Legend Elite-1K-HE, Coherent, USA; pulse width: 104 fs; repetition rate: 1 kHz; wavelength: 800 nm) was used to induce polymer self-growth. The laser beam was guided onto the biaxially stretched silicone membrane surface by a galvoscanner system (SCANLAB, Germany). Scanning paths were designed in AutoCAD 2019 and exported as dxf files, which were then imported into Samlight (SCANLAB) for laser control. Laser scribing was conducted either continuously or intermittently to locally release material stress. The number of laser scans was controlled by Samlight software, while laser power and scanning speed were fixed at 50 mW and 50 mm/s, respectively. To reduce the minimum feature size, the laser was focused using a 20X objective lens (OLYMPUS, Japan), and the sample was translated by a motorized 2D stage (MLS203-1, Thorlabs, USA), resulting in micro-pillars with minimum diameters of 15 µm.

Characterization

Side- and top-view optical images and videos of micropillars were recorded by a CCD (Mindvision, Chnia) equipped with optical lenses. Due to the size constraints of the SEM chamber, the stretched membrane was fixed onto a rigid plastic plate with screws, then trimmed for SEM imaging (JSM-6700F, JEOL, Japan). Laser confocal microscopy was performed using OLS5000 (OLYMPUS, Japan). The fingertip contact force on Braille micropillars was measured by a precise force sensor under the stage (HZC-T, Chengying Sensor Co., Ltd. Bengbu, China).

Data availability

All the data that support the findings of this study are included in the Article and its Supplementary Information. Source data are available via Figshare at https://doi.org/10.6084/m9.figshare.31331896. All data are available from the corresponding author upon request.

References

1. Marvi, H., Cook, J. P., Streator, J. L. & Hu, D. L. Snakes move their scales to increase friction. *Biotribology* **5**, 52–60 (2016).
2. Rafsanjani, A., Zhang, Y., Liu, B., Rubinstein, S. M. & Bertoldi, K. Kirigami skins make a simple soft actuator crawl. *Sci. Robot.* **3**, eaar7555 (2018).
3. Hu, D. L., Nirody, J., Scott, T. & Shelley, M. J. The mechanics of slithering locomotion. *Proc. Natl. Acad. Sci.* **106**, 10081–10085 (2009).
4. Autumn, K. et al. Adhesive force of a single gecko foot-hair. *Nature* **405**, 681–685 (2000).
5. Tian, Y. et al. Adhesion and friction in gecko toe attachment and detachment. *Proc. Natl. Acad. Sci.* **103**, 19320–19325 (2006).
6. Boesel, L. F., Greiner, C., Arzt, E. & Del Campo, A. Gecko-inspired surfaces: a path to strong and reversible dry adhesives. *Adv. Mater.* **22**, 2125–2137 (2010).
7. Xu, C. Colorado Escobar, M. & Gorodetsky, A. A. Stretchable Cephalopod-Inspired Multimodal Camouflage Systems. *Adv. Mater.* **32**, 1905717 (2020).
8. Pikul, J. et al. Stretchable surfaces with programmable 3D texture morphing for synthetic camouflaging skins. *Science* **358**, 210–214 (2017).
9. Bogdanov, G. et al. Gradient refractive indices enable squid structural color and inspire multispectral materials. *Science* **388**, 1389–1395 (2025).

10. Zhao, B. et al. Overcoming challenges: Advancements in cutting techniques for high strength-toughness alloys in aero-engines. *Int. J. Extrem. Manuf.* **6**, 062012 (2024).
11. Xia, Y. & Whitesides, G. M. Soft lithography. *Angew. Chem. Int. Ed.* **37**, 550–575 (1998).
12. Li, W. et al. Crack engineering for the construction of arbitrary hierarchical architectures. *Proc. Natl. Acad. Sci.* **116**, 23909–23914 (2019).
13. Mao, M. et al. 3D printing in space: from mechanical structures to living tissues. *Int. J. Extrem. Manuf.* **6**, 023001 (2024).
14. Halatek, J. & Frey, E. Rethinking pattern formation in reaction–diffusion systems. *Nat. Phys.* **14**, 507–514 (2018).
15. Grzybowski, B. A., Bishop, K. J., Campbell, C. J., Fialkowski, M. & Smoukov, S. K. Micro-and nanotechnology via reaction–diffusion. *Soft Matter* **1**, 114–128 (2005).
16. Xue, L. et al. Light-regulated growth from dynamic swollen substrates for making rough surfaces. *Nat. Commun.* **11**, 1–9 (2020).
17. Chen, D. et al. Homeostatic growth of dynamic covalent polymer network toward ultrafast direct soft lithography. *Sci. Adv.* **7**, eabi7360 (2021).
18. Li, T. et al. Micropatterns fabricated by photodimerization-induced diffusion. *Adv. Mater.* **33**, 2007699 (2021).
19. Yan, S. et al. Deformation-induced photoprogrammable pattern of polyurethane elastomers based on poisson effect. *Adv. Mater.* **36**, 2307445 (2024).
20. Yan, S. et al. Photo-directed growth of surface micro-patterns on photosensitive semicrystalline polymers. *Adv. Funct. Mater.* **34**, 2409112 (2024).
21. Wang, H. et al. Transpiration-induced self-growth of texture hydrogel surfaces. *Angewandte Chemie International Edition*, **63**, e202407125 (2024).
22. Mu, Q. et al. Force-triggered rapid microstructure growth on hydrogel surface for on-demand functions. *Nat. Commun.* **13**, 6213 (2022).
23. Gao, X. et al. Micropattern fabricated by acropetal migration controlled through sequential photo and thermal polymerization. *Small*, **20**, 2403099 (2024).
24. Xiong, X., Wang, H., Xue, L. & Cui, J. Self-growing organic materials. *Angew. Chem. Int. Ed.* **62**, e202306565 (2023).
25. Zhou, X. et al. Reversibly growing crosslinked polymers with programmable sizes and properties. *Nat. Commun.* **14**, 3302 (2023).
26. Li, T. et al. Photo-induced spatial gradient network for shape memory polymer with pattern-memorizing surface. *Mater. Horiz.* **9**, 3078–3086 (2022).
27. Xue, J. et al. Self-growing photonic composites with programmable colors and mechanical properties. *Nat. Commun.* **13**, 7823 (2022).
28. Wang, H. et al. Alternating growth for InSitu post-programing hydrogels' sizes and performance. *Adv. Funct. Mater.* **33**, 2212402 (2023).
29. Fang, Y. et al. Orthogonal growth for fabricating hydrogel sensors and circuit boards with in situ post-tunable performance. *Adv. Funct. Mater.* **32**, 2206222 (2022).
30. Yang, Y. et al. Femtosecond laser regulated ultrafast growth of mushroom-like architecture for oil repellency and manipulation. *Nano Lett.* **21**, 9301–9309 (2021).
31. Zhang, Y. et al. Localized self-growth of reconfigurable architectures induced by a femtosecond laser on a shape-memory polymer. *Adv. Mater.* **30**, 1803072 (2018).
32. Gent, A. N. *Engineering with rubber: how to design rubber components*. (Carl Hanser Verlag GmbH Co KG, 2012).
33. Treloar, L. R. G. The Physics of Rubber Elasticity. Oxford University Press, Oxford (1975).
34. Qi, H. J. & Boyce, M. C. Stress–strain behavior of thermoplastic polyurethanes. *Mech. Mater.* **37**, 817–839 (2005).
35. Arruda, E. M. & Boyce, M. C. A three-dimensional constitutive model for the large stretch behavior of rubber elastic materials. *J. Mech. Phys. Solids* **41**, 389–412 (1993).
36. Barlow-Brown, F., Barker, C. & Harris, M. Size and modality effects in Braille learning: Implications for the blind child from pre-reading sighted children. *Br. J. Educ. Psychol.* **89**, 165–176 (2019).
37. Saikot, M. M. H. & Sanim, K. R. I. Refreshable braille display with adjustable cell size for learners with different tactile sensitivity. *IEEE Trans. Haptics* **15**, 582–591 (2022).
38. Motto Ros, P. et al. A new dynamic tactile display for reconfigurable braille: implementation and tests. *Front. Neuroeng.* **7**, 6 (2014).
39. Watanabe, T., Oouchi, S., Yamaguchi, T., Shimojo, M. & Shimada, S. In *2006 International Conference of the IEEE Engineering in Medicine and Biology Society*. 4936-4940 (IEEE).
40. Mensah, B., Kim, H. G., Lee, J.-H., Arepalli, S. & Nah, C. Carbon nanotube-reinforced elastomeric nanocomposites: a review. *Int. J. Smart Nano Mater.* **6**, 211–238 (2015).
41. Kumar, V. et al. Silicone rubber composites reinforced by carbon nanofillers and their hybrids for various applications: A review. *Polymers* **13**, 2322 (2021).

Acknowledgements

This work was supported by the Key Research and Development Program of the Ministry of Science and Technology (Grant Nos. 2023YFB4604100 (Y.L.) and 2024YFB4610700 (Y.H.)), the National Natural Science Foundation of China (Grant Nos. 52375582 (Y.H.), 52105492 (Y.Z.), 62375073 (S.W.) and 62461160305 (D.W.)), the National Natural Science Foundation of Anhui Province (2508085ME104 (Y.Z.)), the Fundamental Research Funds for the Central Universities of China (JZ2025HGTB0211 (Y.Z.), PA2025IISL0101 (Y.Z.) and WK2090000088 (Y.H.)) and the Hong Kong Research Grants Council (No. N_CUHK472/24 (L.Z.)). The analysis work of this article was partially carried out at the Instrumental Analysis Center, Hefei University of Technology.

Author contributions

Y.Z., Y.H., and S.W. conceived the research and designed the experiments. Y.Z., N.Z., Z.C., Z.Z., T.W., R.X., K.L., Z.L., and Y.L. conducted the experiments and carried out the simulations. Y.H., D.W., L.W., J.L., L.Z., and J.C. supervised the project. All authors analyzed the data and wrote the paper.

Competing interests

The authors declare no competing interests.

Additional information

Supplementary information The online version contains supplementary material available at https://doi.org/10.1038/s41467-026-70098-8.

Correspondence and requests for materials should be addressed to Sizhu Wu or Yanlei Hu.

Peer review information *Nature Communications* thanks Jiaxi Cui and Guoqiang Li for their contribution to the peer review of this work. A peer review file is available.

---

[1]Anhui Province Key Laboratory of Measuring Theory and Precision Instrument, School of Instrument Science and Opto-Electronics Engineering, Hefei University of Technology, Hefei, China. [2]CAS Key Laboratory of Mechanical Behavior and Design of Materials, Department of Modern Mechanics, University of Science and Technology of China, Hefei, China. [3]CAS Key Laboratory of Mechanical Behavior and Design of Materials, Department of Precision Machinery and Precision Instrumentation, University of Science and Technology of China, Hefei, China. [4]Key Laboratory of Testing Technology for Manufacturing Process of Ministry of Education, Southwest University of Science and Technology, Mianyang, China. [5]State Key Laboratory of Extreme Photonics and Instrumentation, Zhejiang Key Laboratory of Intelligent Electromagnetic Control and Advanced Electronic Integration, Zhejiang University, Hangzhou, China. [6]Department of Mechanical and Automation Engineering, The Chinese University of Hong Kong, Hong Kong, SAR, P.R. China. [7]Department of Obstetrics and Gynecology, The First Affiliated Hospital of USTC, Division of Life Sciences and Medicine, University of Science and Technology of China, Hefei, Anhui, China. [8]These authors contributed equally: Yachao Zhang, Nian Zhang. ✉e-mail: sizhuwu@hfut.edu.cn; huyl@ustc.edu.cn